

Effective Field Theory Approach to Scattering of Dark Matter in XENON100 Detector 225 live days run

We report on WIMP search results in the XENON100 detector using a non-relativistic effective field theory (EFT) approach. The data from scientific run II (34 kg * 224.6 live days) was re-analyzed, with the searched recoil energy range extended from previous analyses up to 6.6-240 keV. The data is found to be compatible with the background-only hypothesis. We present 90% confidence level exclusion limits on the coupling constants of EFT operators c_i using a binned profile likelihood method. We also consider the case of inelastic WIMP scattering, where incident WIMPs may up-scatter off Xenon nuclei to a higher mass state, and set exclusion limits on this model as well. The presented limits are to date the strongest published limits from direct detection experiments.

Keywords: Dark Matter, EFT, Xenon

I. INTRODUCTION

Astrophysical and cosmological observations provide strong evidence that 27% of the mass-energy of the universe is made out of Dark Matter (DM), a non-luminous, non-baryonic, and non-relativistic particle, the nature of which is yet unknown [1]. Many well-motivated theoretical extensions of the Standard Model of particle physics predict the existence of one or more particles with the required properties, with masses typically of the order of the weak scale. Such particles are collectively known as Weakly Interacting Massive Particles(WIMPs) [2]. The hypothesis that dark matter is constituted primarily of WIMPs is currently being tested by many experiments, either indirectly by searching for evidence of their possible decay or annihilation in astrophysical processes, by searching for evidence of their direct production at collider experiments, or by directly measuring the rare scattering of astrophysical WIMPs from target nuclei in Earth-based laboratories. We report on a search of this last kind. Although some such experiments have reported potential evidence for WIMPs in the mass range of 6-30 GeV/ c^2 [3-6], these results appear to conflict with null results from other experiments [7-9].

The traditional approach for computing predictions of the rate of WIMP-nucleon scattering has been to take only leading-order terms in a WIMP-nucleon effective theory (EFT) with a very simple treatment of nuclear structure [10]. This leads to two main types of interactions, which are commonly labelled “Spin Independent” (SI) and “Spin Dependent” (SD), however in recent years many authors have been pointed out that in certain theories these interactions may be suppressed or nonexistent, such that otherwise subleading interactions may dominate the scattering process. To account for this possibility in a systematic way a more sophisticated EFT approach has been developed [11-13], which takes into account all leading-order and next-to-leading order operators emerging from an effective Lagrangian describing the WIMP-nucleus interaction. In this framework new operators associated with different types of nuclear responses are introduced along with the standard SI and SD ones, resulting in a set of fourteen operators \mathcal{O}_i which may each couple independently to protons and neutrons. In Eq. 1 we list these operators following the convention

from [12]. The operators depend explicitly on 4 quantities: \vec{v}^\perp , the relative velocity between the WIMP and the nucleon, \vec{q} , the momentum transferred in the scattering event, and \vec{S}_χ , \vec{S}_N , the WIMP and nucleon spins. \mathcal{O}_2 is not considered here as it cannot be obtained from a relativistic operator at leading order.

$$\begin{aligned}
 \mathcal{O}_1 &= 1_\chi 1_N \\
 \mathcal{O}_3 &= i\vec{S}_N \cdot (\frac{\vec{q}}{m_N} \times \vec{v}^\perp) \\
 \mathcal{O}_4 &= \vec{S}_\chi \cdot \vec{S}_N \\
 \mathcal{O}_5 &= i\vec{S}_\chi \cdot (\frac{\vec{q}}{m_N} \times \vec{v}^\perp) \\
 \mathcal{O}_6 &= (\vec{S}_\chi \cdot \frac{\vec{q}}{m_N})(\vec{S}_N \cdot \frac{\vec{q}}{m_N}) \\
 \mathcal{O}_7 &= \vec{S}_N \cdot \vec{v}^\perp \\
 \mathcal{O}_8 &= \vec{S}_\chi \cdot \vec{v}^\perp \\
 \mathcal{O}_9 &= i\vec{S}_\chi \cdot (\vec{S}_N \times \frac{\vec{q}}{m_N}) \\
 \mathcal{O}_{10} &= i\vec{S}_N \cdot (\frac{\vec{q}}{m_N}) \\
 \mathcal{O}_{11} &= i\vec{S}_\chi \cdot (\frac{\vec{q}}{m_N}) \\
 \mathcal{O}_{12} &= \vec{S}_\chi \cdot (\vec{S}_N \times \vec{v}^\perp) \\
 \mathcal{O}_{13} &= i(\vec{S}_\chi \cdot \vec{v}^\perp)(\vec{S}_N \times \frac{\vec{q}}{m_N}) \\
 \mathcal{O}_{14} &= i(\vec{S}_\chi \times \frac{\vec{q}}{m_N})(\vec{S}_N \cdot \vec{v}^\perp) \\
 \mathcal{O}_{15} &= -(\vec{S}_\chi \times \frac{\vec{q}}{m_N})[(\vec{S}_N \times \vec{v}^\perp) \cdot \frac{\vec{q}}{m_N}]
 \end{aligned} \tag{1}$$

Unlike the more commonly studied types of interaction (SI,SD), which are not suppressed when $\vec{q} \rightarrow 0$ and for which the scattering rate on nucleons is expected be largest for low energy nuclear recoils, some of the new EFT operators depend explicitly on \vec{q} and so their interaction cross section is suppressed for low momentum transfers. Consequently, their scattering rate peaks at non-zero nuclear recoil energy, which for sufficiently high WIMP masses may even occur outside typical analysis

windows (< 43 keV) which are designed to search for SI and SD interactions (see Figure 1). Due to this theoretical bias high energy nuclear recoil energies have remain unexplored in many experiments.

Another typical assumption that can be relaxed is that WIMPs should scatter elastically with nuclei, however there exist dark matter models in which the incoming and outgoing WIMPs have different mass states [14] separated by a keV-scale splitting. In the case where the outgoing state is more massive than the incoming state the cross section for low recoil energies can again be suppressed, this time by the scattering kinematics. Recently an inelastic adaptation of the EFT operator framework discussed above was developed [15]. In this case the operators presented in 1 are modified such that $\vec{v}_{inelastic}^\perp = \vec{v}_{elastic}^\perp + \frac{\delta_m}{|\vec{q}|^2} \vec{q}$. We discuss this case further in section III C 2.

The EFT framework of [11] is constructed at the WIMP-nucleon level and so each operator may be present independently for protons and neutrons, though UV models can of course correlate their couplings. The full EFT thus has 28 coupling parameters in addition to the WIMP mass, and, in the inelastic case, a mass splitting δ . The parameter space is thus too large to explore in full, so we take a similar approach to the SI/SD case and characterize the experimental limit by assuming only one active operator at a time, with the coupling to protons and neutrons for that operator set equal (the “isoscalar” case). However, to facilitate the full exploitation of these results by the community, we provide in supplementary material a set of tools for converting any theoretical recoil spectrum dR/dE into an accurate event rate prediction for this analysis, including all detector response and analysis efficiency effects. This may help to set a mildly conservative but quite accurate limit on arbitrary models in the full EFT parameter space, or indeed any other particle dark matter model for which one can supply the expected recoil spectrum.

In this paper, motivated by these EFT extensions of the standard WIMP framework, we report on an analysis extending the searched recoil energy range up to 240 keV for the first time in XENON100 experiment, and present exclusion limits on all operators for both the elastic and the inelastic WIMP cases.

II. THE XENON100 DETECTOR

The XENON100 detector is a cylindrical dual-phase xenon (liquid and gas) time projection chamber (TPC). It is installed at the Laboratori Nazionali del Gran Sasso (LNGS) in Italy and hosts 161 kg of liquid xenon (LXe), of which 62 kg function as the active target [16]. The detector consists of a total of 178 1-inch square Hamamatsu R8520-AL photomultiplier tubes (PMTs) employed in two arrays, one in the gas phase at the top of the TPC, and the other at the bottom, immersed in the LXe.

A particle interacting with the LXe deposits energy

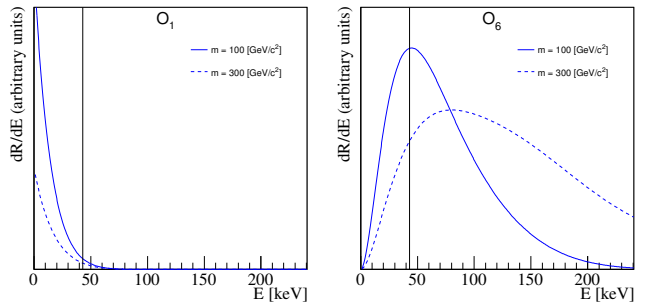


FIG. 1. Example EFT recoil spectra for elastic scattering of spin-1/2 WIMPs on Xenon nuclei (weighted according to the isotope abundances in the XENON100 experiment). Left(right) shows the predicted spectra for EFT operator $O_1(O_6)$. The normalization is controlled by the coupling coefficient of each EFT operator and the experimental exposure (left arbitrary in this figure). The solid vertical line at 43 keV shows the approximate division between the two signal regions used in this analysis (30 PE in cS1). As shown, the standard SI (O_1) spectrum is concentrated mainly in the already explored energy region. However, some EFT operators, for certain WIMP masses, predict a significant fraction of recoil events above the upper energy cut used in the standard spin-independent analysis, motivating an extension of this cut. The highest recoil energy shown in the plots, 240 keV, roughly corresponds to the extended cS1 cut of 180 PE used in this analysis.

that creates both excited and ionized molecular states. De-excitation of these excited molecular states induce a prompt scintillation signal ($S1$), while electrons from ionization processes are drifted in an electric field of 530V/cm towards the liquid-gas interface where they are extracted using a larger electric field of ~ 12 kV/cm. These electrons generate a proportional scintillation, which is called $S2$. The spatial distribution of the $S2$ signal on the top PMT array, together with the time difference between $S1$ and $S2$ signals, provides respectively X-Y and Z position information for each interaction, allowing 3D position reconstruction to be achieved.

Interactions in different positions cover different solid angles with respect to the PMT array, which leads to a position-dependent $S1$ signal. At the same time, warping of the top meshes and the absorption of electrons by residual impurities lead to a position-dependent $S2$ signal. To take these effects into account a correction is applied based on a light collection efficiency (LCE) map. The corrected signals (cS1,cS2) are spatially independent and uniform to all interactions [16].

The $S2/S1$ ratio is known to differ between nuclear recoil (NR) and electronic recoil (ER) interactions, and is thus used as a discriminating variable between a WIMP signal and ER background. The logarithm of this ratio, $\log(cS2/cS1)$ is referred later in the text as the y discriminating variable.

145

III. DATA ANALYSIS

146 In this work we re-analyze scientific run II data
 147 recorded between February 2011 and March 2012, corre-
 148 sponding to 224.6 live days. The characterization of the
 149 detector response to ER interactions is performed using
 150 dedicated calibration campaigns with ^{60}Co and ^{232}Th ra-
 151 dioactive sources, while the response to NR interactions
 152 is performed using $^{241}\text{AmBe}$ calibration campaigns.

153 This work extends the previous results [7, 17], referred
 154 to in the following as the low energy channel, with a
 155 new study exploring the recoil energy range between 43-
 156 240 keV. The data analysis is divided into two mutually
 157 exclusive channels, one optimized for low energies and
 158 ranging from 3-30 PE in cS1 (lowE), the other optimized
 159 for high energies recoils ranging from 30-180 PE in cS1
 160 (highE). These two analysis are then statistically com-
 161 bined. The regions of interests (ROI) in these two chan-
 162 nels, in which we search for dark matter events, are shown
 163 in Figure 3 and further described in the following sec-
 164 tions.

165

A. Low Energy

166 This analysis channel relies on the re-analysis of run II
 167 data described in [7]. The region of interest, the back-
 168 ground expectation models, data selections and their ac-
 169 ceptances are mostly unchanged and so are only briefly
 170 summarized here. Differences with respect to said results
 171 are highlighted when present.

172 The region of interest for this channel spans the
 173 $(y, cS1)$ -plane and is shown in Figure 3. The lower bound
 174 on y corresponds to a 3σ acceptance quantile (as a func-
 175 tion of cS1) of a 20 GeV WIMP mass signal model, while
 176 the upper bound is fixed at $y=2.7$. The range in cS1 is
 177 selected as 3 to 30 PE. This ROI is further divided into
 178 WIMP mass dependent sub-regions (also called bands)
 179 arranged in a way to achieve constant expected signal
 180 density in each region, as described in [7].

181 Other than falling into the ROI, an event should fulfill
 182 several additional selection criteria such as data quality
 183 and noise cuts, an event veto in the presence of energy
 184 release in the outer LXe shield, energy selection and S2
 185 threshold cuts, selection of single-scatter events, and a
 186 predefined fiducial volume of 34 kg. More details on these
 187 selection criteria and their relative WIMP signals accep-
 188 tances can be found in [7, 18].

189 In addition, this analysis channel uses the post un-
 190 blinding cuts and data reprocessing described in [7]. To
 191 summarise the main features, data is reprocessed with
 192 an improved (S1,S2) classification algorithm, and a new
 193 cut targeted to suppress data periods with non-random
 194 occurrence of lone-S1 (an S1 without any correlated S2)
 195 events is applied. Finally, this channel does not employ
 196 a variable lower S1 threshold as a function of the event
 197 position, but a fixed lower threshold cut on cS1 at 3 PE,
 198 converse to what was reported in [7].

199 The expected background is modeled separately for ER
 200 and NR contributions which are then scaled to exposure
 201 and added together. The NR background is estimated
 202 by Monte Carlo simulation and accounts for the radio-
 203 genic and cosmogenic neutron contributions [19]. The
 204 ER background is parametrized as the linear combina-
 205 tion of Gaussian-shaped and non-Gaussian components.
 206 The first is obtained via a parametric fit of the ^{60}Co and
 207 ^{232}Th calibration data, as discussed in [17]. In contrast,
 208 the expected distribution and yields for the non-Gaussian
 209 population, consisting of anomalous events such as those
 210 presenting incomplete charge collection or accidental co-
 211 incidence of uncorrelated S1s and S2s, are evaluated via
 212 dedicated techniques described in [7].

213 Systematic uncertainties on the background model
 214 arising from the Gaussian parametrized fit plus the nor-
 215 malisations of the NR and non-Gaussian components
 216 have been evaluated. It has been shown that the prop-
 217 agated errors are conservatively within the calibration
 218 samples (used to assess the model) statistical uncer-
 219 tainties, thus chosen as the overall uncertainty of the
 220 model [7].

221

B. High Energy

222 This analysis channel targets high energy nuclear re-
 223 coils and is the focus of this work. The data selection
 224 criteria we use are based on the criteria described in de-
 225 tail in [18], which were optimized for high acceptance to
 226 low energy nuclear recoils. Most of these selection criteria
 227 (cuts) were found to be fully compatible with (or easily
 228 extended) to high energy depositions, however some re-
 229 quired more comprehensive studies, which are described
 230 in what follows.

231 The width of an S2 pulse increases with the depth (z)
 232 of the interaction. This is due to the diffusion of the
 233 electron cloud during its propagation towards the gate
 234 grid. Low energy S2 events show larger spread due to
 235 low statistics of drifted ionization electrons, hence the
 236 cut was previously defined in an energy-dependent way.
 237 However for recoil energies which are high enough, as in
 238 this channel, this energy dependency is not valid. We
 239 therefore use here a cut on the S2 width which is a func-
 240 tion of the depth of the interaction alone.

241 As a WIMP will interact only once in the detector, we
 242 remove events which have more than one S2. We adopt
 243 here a cut that is more suitable to higher energies and
 244 demands a single S2 in a $160 \mu\text{s}$ window, instead of a
 245 linear dependence between the second S2 size and the
 246 first.

247 To define the interaction's exact location, we use sev-
 248 eral algorithms, one of which is based on a Neural Net-
 249 work (NN) [18]. The NN was not trained to recognize
 250 high energy ER events and therefore a cut on the NN
 251 score is not suitable for this analysis. We therefore dis-
 252 card this cut but keep all other cuts on position recon-
 253 struction quality, which is sufficient to ensure a correct

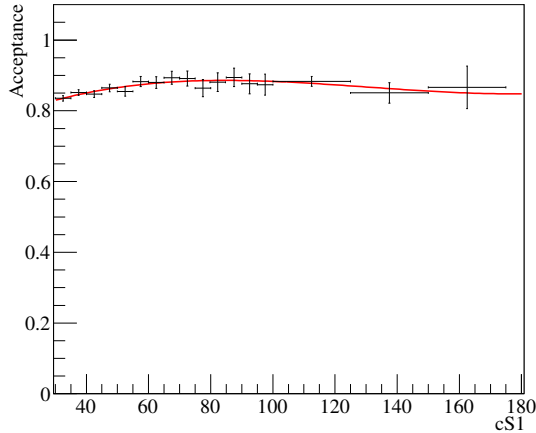


FIG. 2. The total acceptance of all cuts used. Data from calibration is shown in black, with a polynomial fit in red.

254 position reconstruction.

255 The total acceptance to WIMP signals is computed
256 based on $^{241}\text{AmBe}$ calibration data as a function of cS1,
257 following the procedure described in [18]. We present this
258 function in Figure 2, where the total acceptance is fitted
259 using a 3rd order polynomial.

260 We define our signal region in the discrimination
261 (y,cS1)-plane using $^{241}\text{AmBe}$ calibration data. The ROI
262 is shown in Figure 3 as blue contour lines: the upper
263 bound is defined such that it is not contaminated from
264 contribution due to xenon excitation lines, the lower is
265 defined as the 3σ acceptance quantile of the $^{241}\text{AmBe}$
266 distribution.

267 We divide our signal region into two bands, con-
268 structed such that the $^{241}\text{AmBe}$ data sample is equally
269 distributed in y between them. The total number of
270 events in each band is ~ 3000 events. The bands are
271 further divided into nine bins. The definition and con-
272 tent of the bins are presented in Table I and in Figure 3.

273 The main source of background results from ER leak-
274 age, therefore we estimate the background distribution
275 in the ROI using ^{60}Co and ^{232}Th calibration samples.
276 Contributions from radiogenic and cosmogenic neutrons,
277 and accidental coincidence, are negligible for such a high
278 energy recoil. In Table I we report the background ex-
279 pectation for each bin in the ROI along with the ob-
280 served events in each bin. Here the background expecta-
281 tion is computed by scaling the calibration sample yield
282 by 6.54×10^{-3} , which is simply the ratio of observed
283 counts to calibration counts in an independent sideband.
284 Note that in the computation of exclusion limits the back-
285 ground normalization is instead fitted to data during hy-
286 pothesis testing, as described in section III D.

#	Band	Energy Range (cS1)	# Background Events	# Data Events
1	upper	30 - 40	23.5	20
2	upper	40 - 50	15.7	17
3	upper	50 - 80	12.4	11
4	upper	80 - 120	1.1	1
5	upper	120 - 150	0.1	1
6	upper	150 - 180	0.08	0
7	lower	30 - 50	0.9	0
8	lower	50 - 90	0.35	0
9	lower	120 - 180	0.18	0

TABLE I. Definitions and contents of the analysis bins for the high energy channel. The expected background counts are calculated by taking the calibration sample and scaling it by 6.54×10^{-3} , which is the ratio of observed counts to calibration counts in a sideband.

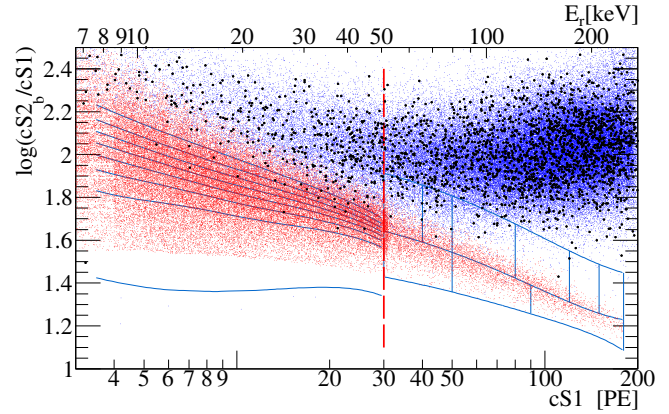


FIG. 3. Summary of regions of interest, backgrounds, and observed data. ER calibration data, namely ^{60}Co and ^{232}Th data is shown as blue dots. NR calibration data ($^{241}\text{AmBe}$) is shown as red dots. Dark matter data is shown as black dots. The red dashed line is the threshold between the low and high energy channels. The lines in blue are the bands. For the low energy channel the shown bands are constructed for a $50 \text{ GeV}/c^2$ WIMP. For the high energy region the 9 analysis bins are presented; the top left bin in this region is bin 1, the top right is bin 6, the bottom left is bin 7 and bottom right is bin 9. In Appendix A we show similar data but for regions above the upper range of this analysis, going up to 1000 PE in cS1, for the sake of curiosity as part of final unblinding of XENON100 data.

C. Signal Model

288 The signal model is produced by taking a theoretical
289 event rate spectrum, the production of which is described
290 in sections III C 1 and III C 2, and applying the analysis
291 acceptance and detector response as described in [18] to
292 obtain the expected event rate in the detector in terms
293 of detector variables (i.e. cS1,cS2). In order to calculate
294 the expected value of the signal in cS1, we use Eq. 2 for
295 both energy regions,

$$\langle cS1 \rangle = E_{nr} \cdot (L_y \mathcal{L}_{eff}) \cdot \left(\frac{S_{nr}}{S_{ee}} \right) \quad (2)$$

where E_{nr} is the recoil energy, L_y is the detector related light yield, \mathcal{L}_{eff} is the scintillation efficiency relative to 122keV_{ee} as a function of E_{nr} , and S_{ee} and S_{nr} are the quenching factors for ER and NR respectively. Aside from E_{nr} and \mathcal{L}_{eff} these parameters have fixed values, namely $L_y = 2.28 \pm 0.04$, $S_{\text{nr}} = 0.95$, and $S_{\text{ee}} = 0.58$. Recoils below 3 keV are assumed to produce no light since \mathcal{L}_{eff} is not measured at these energies. For details of the physics behind these parameters and the construction of the signal PDF please see [7, 18].

The expected cS2 signal is computed following [20] using Eq. 3 for the lowE region only,

$$\langle cS2_{\text{bottom}} \rangle = E_{\text{nr}} Q_y Y \quad (3)$$

where $Y = 8.27 \pm 0.26$ is the amplification factor determined from the detector response to single electrons [21], and Q_y is the charge yield as a function of E_{nr} . Note that as some of the top PMTs saturate we use only the bottom PMT for energy scale in S2. Applying the detector and PMT responses, and the acceptance as in [7], defines the lowE signal model over the region $3\text{PE} < \text{cS1} < 30\text{PE}$, with $cS2_b > 73.5\text{PE}$.

Eq. 3 hides a small subtlety. The actual $cS2_{\text{bottom}}$ PDF is composed of two pieces, a Poisson term associated with the initial charge liberation and a Gaussian term associated with the PMT response and other detector effects:

$$p_{S2}(cS2_b | E) = \sum_{N'} P_{\text{pmt}}(cS2_b | Y N', \sigma_Y \sqrt{N'}) \cdot \text{Pois}(N' | \mu_Q) \quad (4)$$

where $\mu_Q = E_{\text{nr}} Q_y$ is the expected number of liberated charges in a nuclear recoil event of energy E , and N' is the actual number of liberated charges, which are unmeasured and thus summed over. The amplification factor Y is applied on the actual number of liberated charges N' , not the expected number μ_Q . Associated with this is the variance of the Gaussian response PDF, $\sigma_Y \sqrt{N'}$, where in this analysis $\sigma_Y = 6.93$.

For the high energy region we can not produce the S2 distribution as the method in [20] is not calibrated for high enough recoil energies. We therefore use the NR calibration data distribution in $\log(cS2_b/cS1)$ to estimate the WIMP one. Above 180PE in cS1 the statistics of ²⁴¹AmBe data is too low to estimate the distribution accurately so this forms the higher bound of this analysis. With the $cS2_b$ distribution determined by this empirical method we require only a prediction of the cS1 distribution. This is obtain from Eq. 2, followed by the application of detector and PMT responses, as well as the acceptance given in 2, which completes the highE signal model definition.

Examples of each for two EFT operators are shown in Figures 4 and 5, with the rate normalized to give 5 events in the total energy range (lowE and highE).

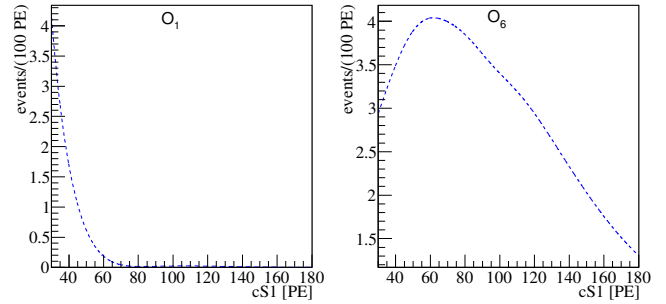


FIG. 4. The expected signal in the high energy region for a 300 GeV/c^2 WIMP mass, Normalized to 5 events. Left(right) is the spectra for $O_1(O_6)$. Notice that for O_1 most of the events are not expected to deposit energy higher than 30 PE whereas for O_6 a large fraction of the events appear in this region.

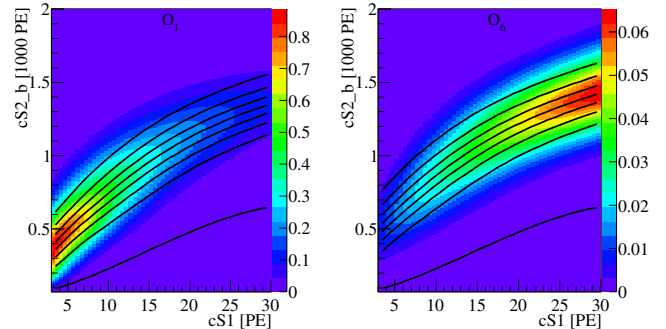


FIG. 5. The expected signal in the low energy region for a 300 GeV/c^2 WIMP mass, Normalized to 5 events. Left(right) is the spectra for $O_1(O_6)$. Notice that for O_1 most of the events are expected to deposit energy lower than 30 PE whereas for O_6 a large fraction of the events do not appear in this region at all. The black lines indicate the bands constructed on this specific event rate, and are dividing the signal into 8 equally distributed signal sub-regions.

1. Elastic Scattering

The expected recoil energy spectrum of each WIMP mass for each EFT operator is calculated using the Mathematica package **DMFormFactor** supplied by Anand et al. [12, 13]. We use standard assumptions as in previous analyses (e.g [7]) regarding the local dark matter density and velocity distribution, namely $\rho_{\text{local}} = 0.3 \text{ GeV/cm}^3$ and a Maxwell-Boltzman distribution with a mean given by the local circular velocity $v_0 = 220 \text{ km/s}$ and cut off at an escape velocity of $v_{\text{esc}} = 544 \text{ km/s}$. The responses of Xe nuclei to a scattering event are computed from one-body density matrices provided with the package, in contrast to the Helm form factors which have been used in previous analyses. These spectra are produced for the seven most abundant Xe isotopes (128,129,130,131,132,134 and 136), combined in proportion to the abundance of these isotopes in the experiment

362 [22], then translated into expected signal rates via the
363 method described above.

364 *2. Inelastic WIMP Scattering*

365 To obtain recoil spectra for WIMP-nucleon scattering
366 for all EFT operators with inelastic kinematics, we use
367 a modified version of `DMFormFactor` provided by Barello
368 et. al. [15]. The authors have modified the original
369 package to enforce the new energy conservation condi-
370 tion $\delta_m + \vec{v} \cdot \vec{q} + |\vec{q}|^2 / 2\mu_N = 0$, primarily by replacing
371 $\vec{v}_{\text{elastic}}^\perp \rightarrow \vec{v}_{\text{inelastic}}^\perp = \vec{v}_{\text{elastic}}^\perp + \frac{\delta_m}{|\vec{q}|^2} \vec{q}$ in the definitions of
372 the EFT and nuclear operators, giving rise to the well-
373 known minimum velocity for scattering

$$v_{\min} = \frac{1}{\sqrt{2m_N E_R}} \left| \frac{m_N E_R}{\mu_N} + \delta_m \right| \quad (5)$$

374 where μ_N is the WIMP-nucleon reduced mass.

375 Assumptions regarding the dark matter halo and nu-
376 clear physics are unchanged. The mass splitting δ_m be-
377 tween dark matter states is varied from 0 to 300 keV,
378 safely beyond the value at which the predicted rate is
379 zero for the entire mass range we consider.

380 *D. Statistical Inference*

381 The statistical interpretation of data is performed by
382 means of a binned profiled likelihood method, in which
383 hypothesis testing relies upon a likelihood ratio test
384 statistic, \tilde{q} , and its asymptotic distributions [23]. The
385 two analysis channels are statistically independent once
386 certain common nuisance parameters are factored out,
387 so we combine them by multiplying their likelihoods
388 together to produce a joint likelihood. Both analysis
389 parametrize the NR relative scintillation efficiency, \mathcal{L}_{eff} ,
390 based on existing measurements [24]. Its uncertainty is
391 the major contributor to energy scale uncertainties and is
392 considered as correlated between the two analysis chan-
393 nels via a separate nuisance likelihood term. Throughout
394 this study, all the parameters related to systematic un-
395 certainties are assumed to be normally distributed.

396 For the low energy channel an extended likelihood
397 function is employed which is very similar to the one
398 reported in [25] and described in detail in [7]. The ROI
399 discriminating (y,cS1)-plane is divided into eight WIMP
400 mass dependent bands where events are counted. This
401 binned approach is extended with the corresponding cS1-
402 projected pdf of each band. The total normalization of
403 the background is fit to data, and an uncertainty is as-
404 signed to the relative normalization of each band accord-
405 ing to the corresponding statistical uncertainty of the cal-
406ibration sample. Signal shape variations due to energy
407 scale uncertainty are modeled via simulation. Addition-
408 ally to \mathcal{L}_{eff} , uncertainties due to the charge yield function
409 Q_y are parametrized as described in [20].

410 The high energy channel analysis employs a binned
411 likelihood function. Observed and expected event yield
412 are compared in the nine ROI (y,cS1)-bins described in
413 section III B. Given the large statistical uncertainty of
414 the background model the above extended likelihood ap-
415 proach is not repeated here. Instead, the MLE of the
416 background expectation in each bin is constrained by the
417 statistical uncertainty of the calibration sample, while
418 the total normalization is fit to the data. Addition-
419 ally, to account for potential mismodeling of the expected
420 background distribution, mainly due to anomalous mul-
421 tiple scatter events, a systematic uncertainty of 20% is
422 assigned independently to each bin. In this channel,
423 uncertainty on the signal acceptance of analysis selec-
424 tions are computed for each signal hypothesis using the
425 parametrized acceptance curve shown in Figure 2. Un-
426 certainties on the signal model (y,cS1) distribution due
427 to $^{241}\text{AmBe}$ sample statistical fluctuations, as well as en-
428 ergy scale shape variation due to \mathcal{L}_{eff} uncertainties, are
429 implemented.

430 **IV. RESULTS**

431 A benchmark region of interest is defined between the
432 upper and lower thresholds in cS1 for each channel. This
433 region is bounded in y space from above by the $^{241}\text{AmBe}$
434 NR mean line and below by the lower 3σ quantile of
435 the AmBe neutron calibration data. The expected back-
436 ground in the region is 3 ± 0.5 (lowE) and 1.41 ± 0.28
437 (highE). The number of DM candidates recorded in this
438 region is 3 (lowE), and 0 (highE). The data is compat-
439 ible with the background-only hypothesis and no excess
440 is found.

441 For the elastic scattering case, a 90% CL_S [26] confi-
442 dence limit is set on the effective coupling constant, c_i ,
443 for all operators and masses in the range of $10 \text{ GeV}/c^2$
444 to $1 \text{ TeV}/c^2$. These limits are shown in Fig. 9 in black,
445 along with limits from CDMS-II Si, CDMS-II Ge and Su-
446 perCDMS [27]. For operators 3 and 8, a full CDMS limit
447 is presented, for all other operators only the limit for a
448 $10 \text{ GeV}/c^2$ and $300 \text{ GeV}/c^2$ are published.

449 For the inelastic scattering case, 90% CL_S confidence
450 limits on the coupling constants are set. Fig. 6 shows
451 limits on the \mathcal{O}_1 (SI) coupling constant as a function
452 of mass splitting and WIMP mass, while Fig. 10 shows
453 limits for all other operators as a function of the mass
454 splitting δ_m with a fixed WIMP mass of $1 \text{ TeV}/c^2$.

455 **V. SUMMARY**

456 We have shown the first analysis of XENON100 data
457 at recoil energies above 43 keV, with the new high energy
458 bound set to 240 keV. We considered in this paper two
459 models which predict interactions in this energy region:
460 an EFT approach for elastic WIMP-nucleon scattering,
461 and a similar EFT approach but considering instead in-

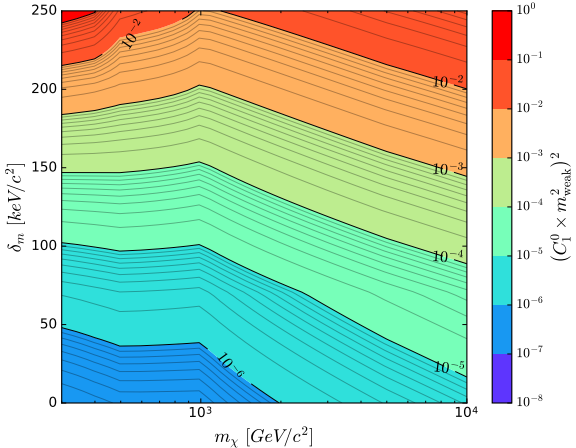


FIG. 6. 90% CL_S limits on the magnitude of the coupling constant for \mathcal{O}_1 , reported as a function of the WIMP mass and mass splitting δ .

462 elastic WIMP-nucleon scattering. The observed data was
 463 compatible with background expectations, and 90% CL_S
 464 exclusion limits were constructed for WIMP masses be-
 465 tween 10-1000 GeV, setting the current strongest limits
 466 from a direct detection experiment on these models.

VI. ACKNOWLEDGMENT

467 Liam Fitzpatrick Spencer Chang

469 Appendix A: Data from Recoil energy up to 1000 PE

470 This analysis is focused on energy recoils up to 240 keV
 471 (180 PE) due to low statistics of NR calibration data. For
 472 completeness, the data for events with recoil energy up
 473 to 1000 PE is presented in 7. The data selection criteria
 474 are the same as those applied for the highE region.

475 Appendix B: Signal model detector response table

476 In this appendix we describe digital tables which can
 477 be used to construct an accurate signal model for this
 478 analysis given any input recoil spectrum dR/dE . A vi-
 479 sualization of the tables is shown in Fig. 8, and in section
 480 B 1 we show a simple example of how to use the supplied
 481 tables in Python. Currently we provide these tables only
 482 for the high E analysis region.

The signal model for the high E analysis region can be
 expressed analytically in the form:

$$\frac{dR}{dcS1} = \int \frac{dR}{dE} \cdot \epsilon_{S1}(cS1) \cdot \epsilon_{S2'}(E) \cdot ps_1(cS1|E) dE \quad (B1)$$

$$= \int \frac{dR}{dE} G(cS1, E) dE \quad (B2)$$

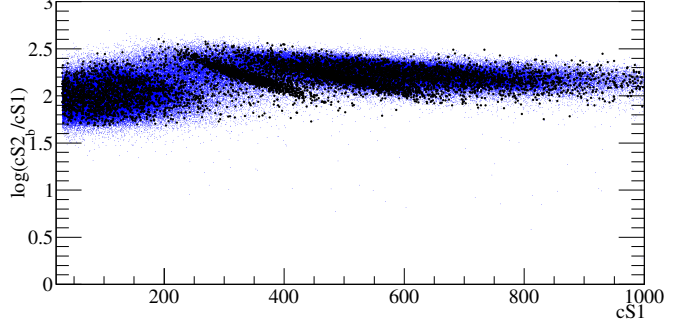


FIG. 7. In blue data from ER calibration (⁶⁰Co and ²³²Th). In black data from dark matter sample. the two large population at 350 PE and 500 PE are the 110 keV and 197 keV excitation lines of ¹⁹F coming from the PTFE walls of the TPC.

483 where $\epsilon_{S1}(cS1)$ and $\epsilon_{S2'}(E)$ represent analysis cut effi-
 484 ciencies, $ps_1(cS1|E)$ encodes detector effects, and dR/dE
 485 gives the theoretically predicted nuclear recoil rate from
 486 WIMP scattering. In the second line we emphasise that
 487 all the detector and analysis effects can be encoded in a
 488 single function $G(cS1, E)$. To make a signal prediction
 489 for the bins in our analysis this expression needs to be
 490 integrated over the appropriate range of $cS1$ for each bin
 491 (and divided by two to account for the banding structure
 492 in $cS2_b$):

$$R_{\text{bin}_i} = \frac{1}{2} \int_{\text{lower}_i}^{\text{upper}_i} \frac{dR}{dcS1} dcS1 \quad (B3)$$

With some simple rearrangement this rate can be written
 in terms of an integral over the detector response function
 G as follows

$$R_{\text{bin}_i} = \frac{1}{2} \int \frac{dR}{dE} \int_{\text{lower}_i}^{\text{upper}_i} G(cS1, E) dcS1 dE \quad (B4)$$

$$= \int \frac{dR}{dE} G'_i(E) dE \quad (B5)$$

493 where in the last line we absorb the factor of 1/2 into
 494 the definition of G'_i . We see here that the signal rate for
 495 each bin can be expressed as an integral over the recoil
 496 spectrum times a detector response function G'_i for that
 497 bin. It is these detector response functions which are
 498 shown in Fig. 8, and which we provide digitally for use
 499 by the community (a low-resolution example is given in
 500 Table II). With these tables it is simple to produce a
 501 signal model for our analysis for any input theoretical
 502 recoil spectrum. The functions G'_i are provided for three
 503 values of the nuisance variable \mathcal{L}_{eff} , namely the median
 504 value and values at $\pm 1\sigma$ in \mathcal{L}_{eff} . From these, along with
 505 the measured background rates given in table I, one may
 506 construct a likelihood which accounts for uncertainties in
 507 \mathcal{L}_{eff} , however simply using the -1σ value produces quite
 508 an accurate prediction and is generally conservative.
 509 Details of how to extract and use the provided G' func-
 510 tions are given in the example of section B 1.

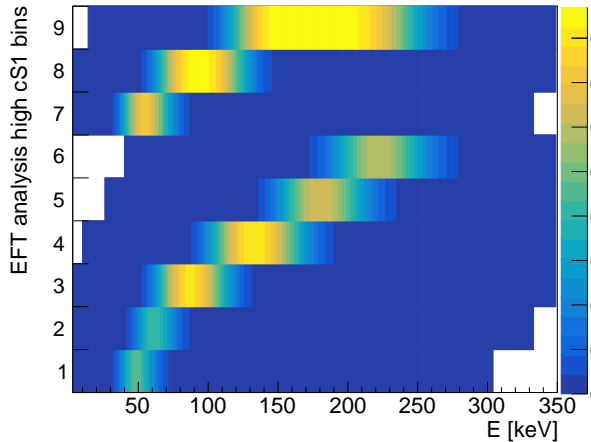


FIG. 8. A visualization of the detector response table for -1σ (i.e. conservative) \mathcal{L}_{eff} , as provided in the supplementary material. The table visualization shows, on the y axis, the bins used for the high E signal region of this analysis. The x axis shows recoil energies, and the colours give the probability density for a recoil of a given recoil energy to produce an event in each analysis bin. To produce a signal model for this analysis, one simply multiplies the table values by dR/dE and integrates over E . The result is the predicted signal rate for each analysis bin.

#	E(keV)	bin 1	bin 2	bin 3	bin 4	bin 5	bin 6	bin 7	bin 8	bin 9
3.00e+00	1.44e-22	2.70e-32	1.23e-42	0.00e+00	0.00e+00	0.00e+00	1.44e-22	1.23e-42	0.00e+00	
1.30e+01	9.21e-09	7.58e-14	1.25e-19	6.21e-40	0.00e+00	0.00e+00	9.21e-09	1.25e-19	0.00e+00	
2.30e+01	1.74e-04	1.07e-07	1.24e-11	1.51e-26	0.00e+00	0.00e+00	1.74e-04	1.24e-11	2.64e-32	
3.30e+01	2.22e-02	2.79e-04	6.56e-07	5.47e-18	8.20e-38	0.00e+00	2.25e-02	6.56e-07	1.71e-22	
4.30e+01	1.59e-01	1.68e-02	3.50e-04	1.89e-12	1.24e-28	1.82e-43	1.76e-01	3.50e-04	4.95e-16	
5.30e+01	2.23e-01	1.21e-01	1.40e-02	1.28e-08	6.89e-22	1.43e-34	3.44e-01	1.40e-02	1.82e-11	
6.30e+01	1.10e-01	2.12e-01	9.84e-02	4.73e-06	5.28e-26	5.47e-17	8.71e-01	9.84e-02	2.59e-08	
7.30e+01	2.77e-02	1.54e-01	2.51e-01	2.58e-04	2.20e-13	5.56e-23	1.82e-01	2.51e-01	4.20e-06	
8.30e+01	4.38e-03	6.14e-02	3.67e-01	4.07e-03	1.36e-10	5.26e-19	6.58e-02	3.71e-01	1.65e-04	
9.30e+01	4.65e-04	1.52e-02	3.96e-01	2.73e-02	2.31e-08	1.01e-18	1.57e-02	4.21e-01	2.44e-03	
1.03e+02	3.40e-05	2.47e-02	3.41e-01	9.81e-02	1.50e-06	6.05e-13	2.50e-03	4.21e-01	1.75e-02	
1.13e+02	1.91e-06	2.89e-04	2.29e-01	2.13e-01	4.09e-05	1.22e-10	2.91e-04	3.74e-01	6.77e-02	
1.23e+02	7.75e-08	2.38e-05	1.14e-01	3.28e-01	5.91e-04	1.16e-08	2.39e-05	2.76e-01	1.66e-01	
1.33e+02	2.18e-09	1.33e-06	3.98e-02	3.97e-01	5.03e-03	5.94e-07	1.33e-06	1.55e-01	2.87e-01	
1.43e+02	5.40e-11	6.21e-08	1.05e-02	4.06e-01	2.41e-02	1.42e-05	6.21e-08	6.64e-02	3.74e-01	
1.53e+02	1.33e-12	2.71e-09	2.23e-03	3.66e-01	7.14e-04	2.17e-09	2.26e-02	4.17e-01		
1.63e+02	2.86e-14	1.00e-10	3.75e-04	2.85e-01	1.51e-01	1.32e-03	1.00e-10	6.04e-03	4.32e-01	
1.73e+02	5.43e-16	3.19e-12	5.09e-05	1.86e-01	2.43e-01	6.76e-03	3.19e-12	1.28e-03	4.34e-01	
1.83e+02	9.29e-18	8.90e-14	15.69e-06	1.01e-01	3.09e-01	2.42e-02	8.90e-14	2.21e-04	4.34e-01	
1.93e+02	1.44e-19	2.21e-15	5.32e-07	4.46e-02	3.23e-01	6.38e-02	2.21e-15	3.14e-05	4.31e-01	
2.03e+02	2.05e-21	4.92e-17	4.23e-08	1.62e-02	2.83e-01	1.29e-01	4.92e-17	3.73e-06	4.28e-01	
2.13e+02	2.71e-23	9.96e-19	2.91e-09	4.89e-03	2.10e-01	2.06e-01	9.96e-19	3.78e-07	4.21e-01	
2.23e+02	3.33e-25	1.85e-20	1.74e-10	1.23e-03	1.31e-01	2.71e-01	1.85e-20	3.29e-08	4.04e-01	
2.33e+02	3.83e-27	3.16e-22	9.25e-12	2.63e-04	6.94e-02	2.99e-01	3.16e-22	2.51e-09	3.69e-01	
2.43e+02	4.16e-29	5.03e-24	4.38e-13	4.80e-05	3.12e-02	2.81e-01	5.03e-24	1.68e-10	3.12e-01	
2.53e+02	4.29e-31	7.48e-26	1.87e-14	7.55e-06	1.20e-02	2.27e-01	7.48e-26	1.00e-11	2.39e-01	
2.63e+02	4.21e-33	1.05e-27	7.23e-16	1.04e-06	3.94e-03	1.58e-01	1.05e-27	5.38e-13	1.62e-01	
2.73e+02	2.39e-35	1.39e-29	2.56e-17	1.25e-07	1.12e-03	9.59e-02	1.39e-29	2.61e-14	9.70e-02	
2.83e+02	3.56e-37	1.74e-31	8.33e-19	1.34e-08	2.77e-04	5.04e-02	1.74e-31	1.15e-15	5.07e-02	
2.93e+02	3.08e-39	2.08e-33	2.51e-20	1.29e-09	6.00e-05	2.31e-02	2.08e-33	4.67e-17	2.31e-02	
3.03e+02	2.58e-41	2.38e-35	7.04e-22	1.11e-10	1.15e-05	9.25e-03	2.38e-35	1.75e-18	9.26e-03	
3.13e+02	2.03e-43	2.61e-37	1.84e-23	8.69e-12	1.95e-06	3.26e-03	2.61e-37	6.06e-20	3.26e-03	
3.23e+02	0.00e+00	2.76e-39	4.54e-25	6.20e-13	2.97e-07	1.01e-03	2.76e-39	1.96e-21	1.01e-03	
3.33e+02	0.00e+00	2.81e-41	1.05e-26	4.06e-14	4.06e-08	2.80e-04	2.81e-41	5.93e-23	2.80e-04	
3.43e+02	0.00e+00	2.72e-43	2.32e-28	2.44e-15	5.04e-09	6.91e-05	2.72e-43	1.69e-24	6.91e-05	

TABLE II. Detector response table using \mathcal{L}_{eff} with constrained scaling parameter set to -1σ value. First column gives recoil energies, subsequent columns give the values of $G'_i(E)$ for each of the 9 high E analysis bins. The sampling is in steps of 10 keV, which is too coarse to give an accurate signal model for very low WIMP masses, but is suitable for the mass range most relevant to our analysis. Higher resolution $G'_i(E)$ functions, and $G'_i(E)$ functions for other values of \mathcal{L}_{eff} , are given in supplementary material [give URL](#).

1. Example code

```

511
512 -----
513 import numpy as np
514 from numpy import newaxis
515 from scipy.interpolate import interp1d
516
517 def TrapI(x,y):
518     """Simple trapezoid integration"""
519     w = x[1:] - x[:-1]
520     h = (y[1:] + y[:-1])/2.
521     return np.sum(w*h, axis=0)
522
523 # Load detector response table
524 data = np.loadtxt("detector_table.dat")
525 E = data[:,0]; Gi = data[:,1:]
526
527 # Load test recoil spectrum (1 TeV WIMP, 06)
528 data = np.loadtxt("06_1TeV.dat")
529 Er = data[:,0]
530 # Input spectra is normalised to coupling^2=1,
531 # rescale to something near limit (1e3)
532 # Also multiply in the appropriate exposure
533 dRdE = data[:,1] * (1e3/1.) * 224.6*34.
534
535 # Interpolate recoil spectrum to table values
536 # Assume spectrum zero outside data given
537 f_dRdE = interp1d(Er,dRdE)
538 dRdE_matched = f_dRdE(E)
539 Ri = TrapI(E[:,newaxis],Gi*dRdE_matched[:,newaxis])
540
541 for i,R in enumerate(Ri):
542     print "bin {0}: rate = {1:.2g}".format(i+1,R)
543
544 Output:
545
546 bin 1: rate = 0.081
547 bin 2: rate = 0.098
548 bin 3: rate = 0.35
549 bin 4: rate = 0.46
550 bin 5: rate = 0.29
551 bin 6: rate = 0.22
552 bin 7: rate = 0.18
553 bin 8: rate = 0.47
554 bin 9: rate = 0.84

```

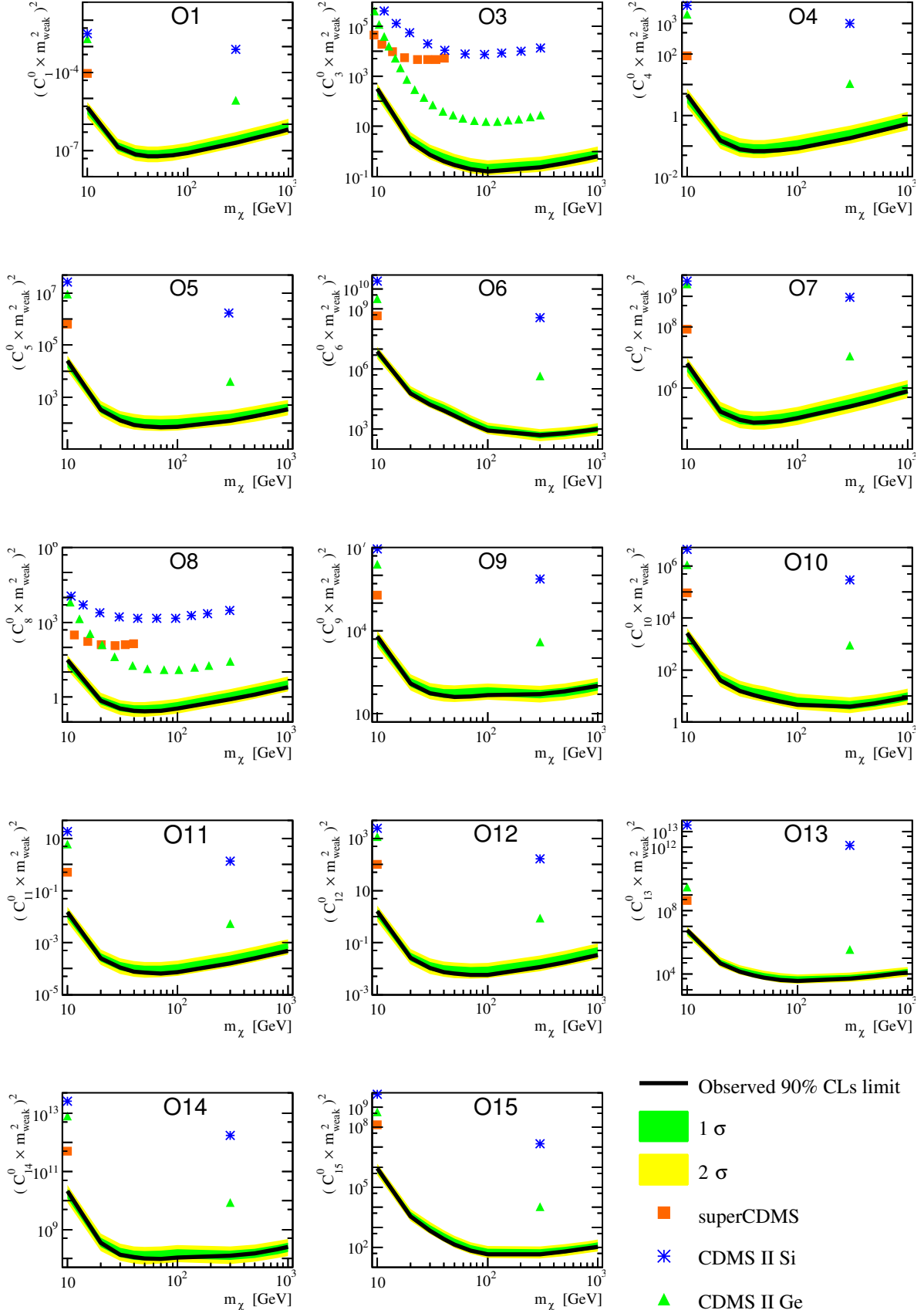


FIG. 9. The XENON100 limits (90% CL_S) on isoscalar dimensionless coupling for all elastic scattering EFT operators. The limits are indicated in solid black. The expected sensitivity is shown in green and yellow(1 σ and 2 σ respectively). Limits from CDMS-II Si, CDMS-II Ge, and SuperCDMS [?] are presented as blue asterisks, green triangles, and orange rectangles, respectively (color online). For operator 3 and 8 a full limit from CDMS is published and indicated by a dashed line in the respective colors.

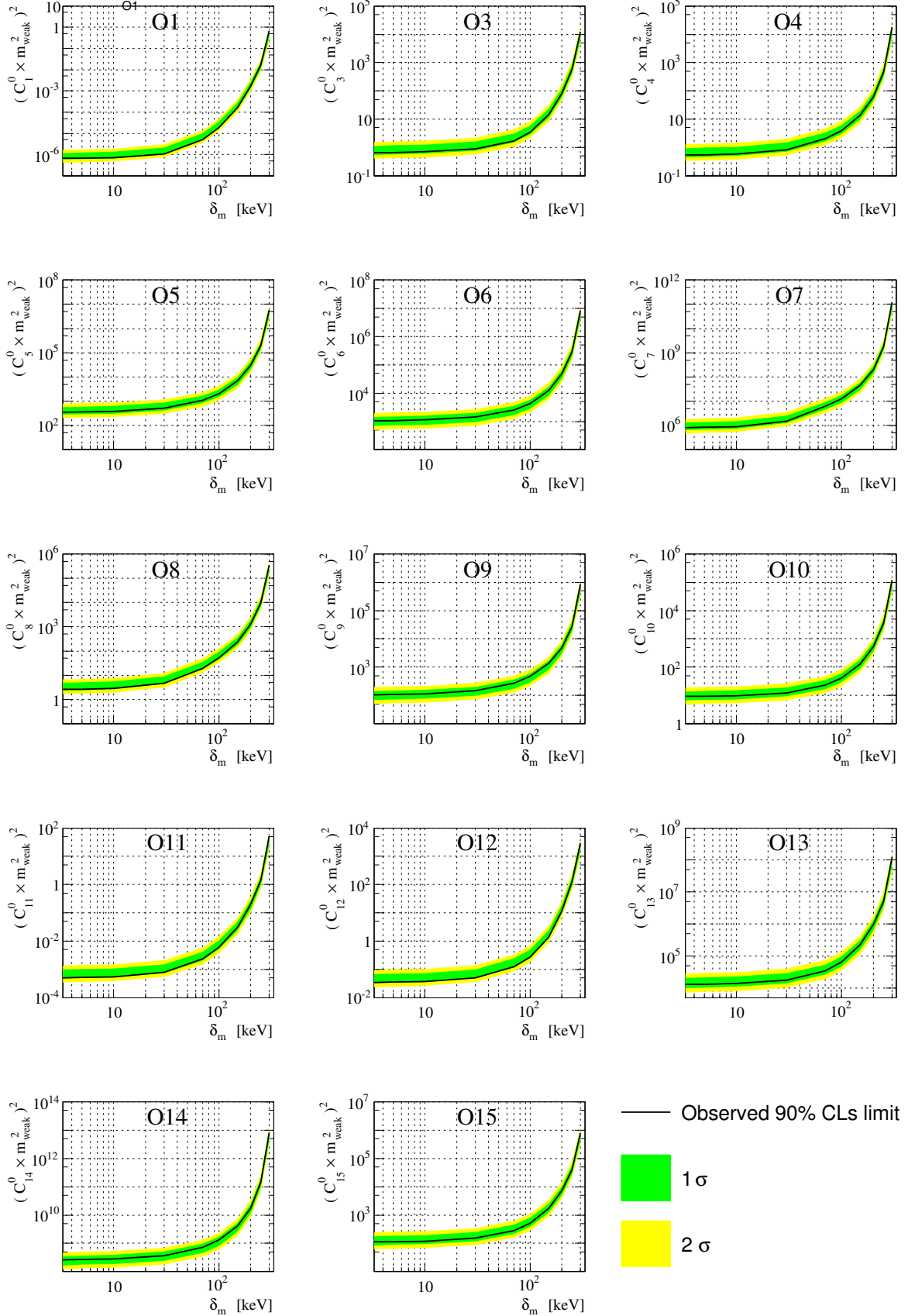


FIG. 10. The XENON100 90% CL_S limits on a 1 TeV/c² WIMP isoscalar dimensionless coupling for all inelastic scattering EFT operators. Limits are indicated in solid black. The expected sensitivity is shown in green and yellow (1 σ and 2 σ respectively).

-
- 556 [1] David Harvey, Richard Massey, Thomas Kitching, Andy 596
 557 Taylor, and Eric Tittley. The nongravitational interac- 597
 558 tions of dark matter in colliding galaxy clusters. *Science*, 598
 559 347(6229):1462–1465, 2015.
- 560 [2] J. Silk et al. *Particle Dark Matter: Observations, Models 600*
 561 and Searches. Cambridge Univ. Press, Cambridge, 2010.
- 562 [3] R. Bernabei et al. New results from dama/libra. *The 602*
 563 European Physical Journal C, 67(1):39–49, 2010.
- 564 [4] C. E. Aalseth et al. Cogent: A search for low-mass dark 604
 565 matter using p -type point contact germanium detectors. 605
Phys. Rev. D, 88:012002, Jul 2013.
- 566 [5] R. Agnese et al. Search for low-mass weakly interact- 606
 567 ing massive particles using voltage-assisted calorimetric 607
 568 ionization detection in the supercdms experiment. *Phys. 608*
Rev. Lett., 112:041302, Jan 2014.
- 569 [6] G. and others Angloher. Results from 730 kg days of the 609
 572 cresst-ii dark matter search. *The European Physical Jour- 610*
 573 nal C, 72(4):1971, 2012.
- 574 [7] E. Aprile et al. XENON100 Dark Matter Results 611
 575 from a Combination of 477 Live Days. *Phys. Rev.*, 612
 576 D94(12):122001, 2016.
- 577 [8] Andi Tan and otrhers. Dark matter results from first 98.7 613
 578 days of data from the pandax-ii experiment. *Phys. Rev.*, 614
 579 Lett., 117:121303, Sep 2016.
- 580 [9] D. S. Akerib et al. Improved Limits on Scattering of 615
 581 Weakly Interacting Massive Particles from Reanalysis of 616
 582 2013 LUX Data. *Phys. Rev. Lett.*, 116(16):161301, 2016.
- 583 [10] J. D. Lewin and P. F. Smith. Review of mathematics, 617
 584 numerical factors, and corrections for dark matter exper- 618
 585 iments based on elastic nuclear recoil. *Astropart. Phys.*, 619
 586 6:87–112, 1996.
- 587 [11] A. Liam Fitzpatrick, Wick Haxton, Emanuel Katz, 620
 588 Nicholas Lubbers, and Yiming Xu. Model Independent 621
 589 Direct Detection Analyses. 2012.
- 590 [12] Nikhil Anand, A. Liam Fitzpatrick, and W. C. Haxton. 622
 591 Weakly interacting massive particle-nucleus elastic scat- 623
 592 tering response. *Phys. Rev.*, C89(6):065501, 2014.
- 593 [13] A. Liam Fitzpatrick, Wick Haxton, Emanuel Katz, 624
 594 Nicholas Lubbers, and Yiming Xu. The Effective 625
 595 Field Theory of Dark Matter Direct Detection. *JCAP*, 626
 596 1302:004, 2013.
- 597 [14] David Tucker-Smith and Neal Weiner. Inelastic dark 627
 598 matter. *Phys. Rev.*, D64:043502, 2001.
- 599 [15] G. Barello, Spencer Chang, and Christopher A. Newby. 628
 600 A Model Independent Approach to Inelastic Dark Matter 629
 601 Scattering. *Phys. Rev.*, D90(9):094027, 2014.
- 602 [16] E. Aprile et al. The XENON100 Dark Matter Experi- 630
 603 ment. *Astropart. Phys.*, 35:573–590, 2012.
- 604 [17] E. Aprile et al. Dark Matter Results from 225 Live Days 631
 605 of XENON100 Data. *Phys. Rev. Lett.*, 109:181301, 2012.
- 606 [18] E. Aprile et al. Analysis of the XENON100 Dark Matter 632
 607 Search Data. *Astropart. Phys.*, 54:11–24, 2014.
- 608 [19] E. Aprile et al. The neutron background of the 633
 609 XENON100 dark matter search experiment. *J. Phys.*, 634
 610 G40:115201, 2013.
- 611 [20] E. Aprile et al. Response of the XENON100 Dark Matter 635
 612 Detector to Nuclear Recoils. *Phys. Rev.*, D88:012006, 636
 613 2013.
- 614 [21] E. Aprile et al. Observation and applications of single- 637
 615 electron charge signals in the XENON100 experiment. *J. 638
 616 Phys.*, G41:035201, 2014.
- 617 [22] E. Aprile et al. Limits on spin-dependent wimp-nucleon 639
 618 cross sections from 225 live days of xenon100 data. *Phys- 640
 619 ical review letters*, 111(2):021301, 2013.
- 620 [23] Glen Cowan, Kyle Cranmer, Eilam Gross, and Ofer 641
 621 Vitells. Asymptotic formulae for likelihood-based tests 642
 622 of new physics. *Eur. Phys. J.*, C71:1554, 2011. [Erratum: Eur. Phys. J.C73,2501(2013)].
- 623 [24] E. Aprile et al. Dark Matter Results from 100 Live Days 643
 624 of XENON100 Data. *Phys. Rev. Lett.*, 107:131302, 2011.
- 625 [25] E. Aprile et al. Likelihood Approach to the First 644
 626 Dark Matter Results from XENON100. *Phys. Rev.*, 645
 627 D84:052003, 2011.
- 628 [26] Alexander L. Read. Modified frequentist analysis of 646
 629 search results (The CL(s) method). In *Workshop on con- 647
 630 fidence limits, CERN, Geneva, Switzerland, 17–18 Jan 648
 631 2000: Proceedings*, pages 81–101, 2000.
- 632 [27] K. Schneck et al. Dark matter effective field theory 649
 633 scattering in direct detection experiments. *Phys. Rev.*, 650
 634 D91(9):092004, 2015.